

NONLINEAR FOURIER ANALYSIS FOR DISCONTINUOUS CONDUCTIVITIES: COMPUTATIONAL RESULTS

K. ASTALA, L. PÄIVÄRINTA, J. M. REYES AND S. SILTANEN

CONTENTS

1. Introduction	2
2. The nonlinear Fourier transform	6
3. Inverse transforms and reconstruction algorithms	8
3.1. The low-pass transport matrix method	8
3.2. The shortcut method	9
3.3. Periodization of the nonlinear inverse transform	10
4. Computational results	12
4.1. Nonlinear Gibbs phenomenon in radial cases	12
4.2. Comparison of the two methods in nonsymmetric cases	20
4.3. Numerical evidence of the transport matrix efficiency	25
5. Conclusion	26
Appendix	27
References	29

ABSTRACT. Two reconstruction methods of Electrical Impedance Tomography (EIT) are numerically compared for nonsmooth conductivities in the plane based on the use of complex geometrical optics (CGO) solutions to D-bar equations involving the global uniqueness proofs for Calderón problem exposed in [Nachman; *Annals of Mathematics* **143**, 1996] and [Astala and Päivärinta; *Annals of Mathematics* **163**, 2006]: the Astala-Päivärinta theory-based *low-pass transport matrix method* implemented in [Astala et al.; *Inverse Problems and Imaging* **5**, 2011] and the *shortcut method* which considers ingredients of both theories. The latter method is formally similar to the Nachman theory-based regularized EIT reconstruction algorithm studied in [Knudsen, Lassas, Mueller and Siltanen; *Inverse Problems and Imaging* **3**, 2009] and several references from there.

New numerical results are presented using parallel computation with size parameters larger than ever, leading mainly to two conclusions as follows. First, both methods can approximate piecewise constant conductivities better and better as the cutoff frequency increases, and there seems to be a Gibbs-like phenomenon producing ringing artifacts. Second, the transport matrix method loses accuracy away from a (freely chosen) pivot point located outside of the object to be studied, whereas the shortcut method produces reconstructions with more uniform quality.

Keywords: Inverse problem, Beltrami equation, Conductivity equation, Inverse conductivity problem, Complex geometrical optics solution, Nonlinear Fourier transform, Scattering transform, Electrical impedance tomography.

1. INTRODUCTION

We study a widely applicable nonlinear Fourier transform in dimension two. We perform numerical tests related to the nonlinear Gibbs phenomenon with much larger cutoff frequencies than before. Furthermore, we compare two computational inverse transformations, called *low-pass transport matrix method* and *shortcut method* in terms of accuracy.

The inverse conductivity problem of Calderón [10] is the main source of applications of the nonlinear Fourier transform we consider. Let $\Omega \subset \mathbb{R}^2$ be the unit disc and let $\sigma : \Omega \rightarrow (0, \infty)$ be an essentially bounded measurable function satisfying $\sigma(x) \geq c > 0$ for almost every $x \in \Omega$. Let $u \in H^1(\Omega)$ be the unique solution to the following elliptic Dirichlet problem:

$$(1.1) \quad \nabla \cdot \sigma \nabla u = 0 \text{ in } \Omega,$$

$$(1.2) \quad u|_{\partial\Omega} = \phi \in H^{1/2}(\partial\Omega).$$

The inverse conductivity problem consists on recovering σ from the Dirichlet-to-Neumann (DN) map or voltage-to-current map defined by

$$\Lambda_\sigma : \phi \mapsto \sigma \frac{\partial u}{\partial \nu} \Big|_{\partial\Omega}.$$

Here ν is the unit outer normal to the boundary. Note that the map $\Lambda : \sigma \mapsto \Lambda_\sigma$ is nonlinear.

The inverse conductivity problem is related to many practical applications, including the medical imaging technique called *electrical impedance tomography* (EIT). There one attaches electrodes to the skin of a patient, feeds electric currents into the body and measures the resulting voltages at the electrodes. Repeating the measurement with several current patterns yields a current-to-voltage data matrix that can be used to compute an approximation Λ_σ^δ to Λ_σ . Since different organs and tissues have different conductivities, recovering σ computationally from Λ_σ^δ amounts to creating an image of the inner structure of the patient. See [41, 12] for more information on EIT and its applications.

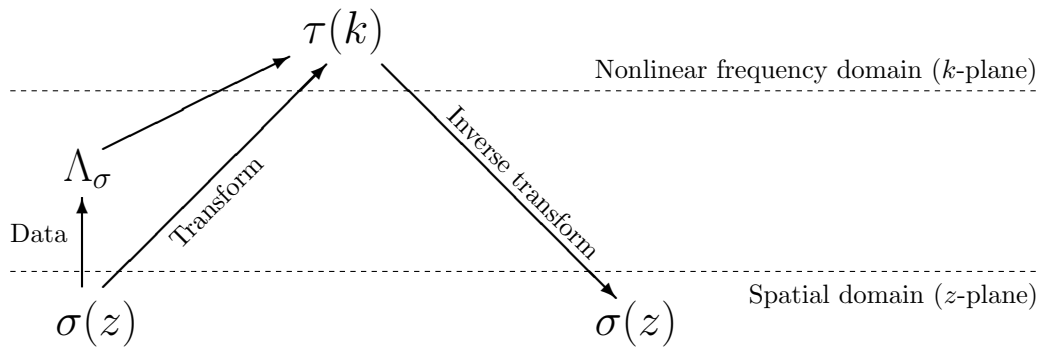
Recovering σ from Λ_σ^δ is a nonlinear and ill-posed inverse problem, whose computational solution requires regularization. Several categories of solution methods have been suggested and tested in the literature; in this work we focus on so-called D-bar methods based on complex geometrical optics (CGO) solutions. There are three main flavors of D-bar methods for EIT:

- Schrödinger equation approach for twice differentiable σ . Introduced by Nachman in 1996 [43], implemented numerically in [45, 40, 31, 30, 34, 41].
- First-order system approach for once differentiable σ . Introduced by Brown and Uhlmann in 1997 [7], implemented numerically in [32, 36, 19].

- Beltrami equation approach assuming no smoothness ($\sigma \in L^\infty(\Omega)$). Introduced by Astala and Päivärinta in 2006 [6], implemented numerically in [5, 4, 3, 41]. The assumption $\sigma \in L^\infty(\Omega)$ was the one originally used by Calderón in [10].

Using these approaches, a number of conditional stability results have been studied for the Calderón problem. The most recent results in the plane were obtained by Clop, Faraco and Ruiz in [13], where stability in L^2 -norm was proven for conductivities on Lipschitz domains in the fractional Sobolev spaces $W^{\alpha,p}$ with $\alpha > 0$, $1 < p < \infty$, and in [15], where the Lipschitz condition on the boundary of the domain was removed. In dimension $d \geq 3$, conditional stability in Hölder norm for just $C^{1+\varepsilon}$ conductivities on bounded Lipschitz domains was proved by Caro, García and the third author in [11] using the method presented in [18].

The three aforementioned D-bar methods for EIT in the two-dimensional case are based on the use of nonlinear Fourier transforms specially adapted to the inverse conductivity problem. Schematically, the idea looks like this:



The main point above is that the nonlinear Fourier transform can be calculated from the infinite-precision data Λ_σ , typically via solving a second-kind Fredholm boundary integral equation for the traces of the CGO solutions on $\partial\Omega$.

In practice one is not given the infinite-precision data Λ_σ , but rather the noisy and finite-dimensional approximation Λ_σ^δ . Typically all we know about Λ_σ^δ is that $\|\Lambda_\sigma - \Lambda_\sigma^\delta\|_Y < \delta$ for some (known) noise level $\delta > 0$ measured in an appropriate norm $\|\cdot\|_Y$. Most CGO-based EIT methods need to be regularized by a truncation $|k| < R$ in the nonlinear frequency-domain as illustrated in Figure 1.

The regularization step results in a smooth reconstruction. This smoothing property of the nonlinear low-pass filter resembles qualitatively the effect of linear low-pass filtering of images. In particular, the smaller R is, the blurrier the reconstruction becomes.

The cut-off frequency R is determined by the noise amplitude δ , and typically R cannot exceed 7 in practical situations. However, it is interesting to understand how the conductivity is represented by its nonlinear Fourier transform. To study this numerically, we compute nonlinear Fourier transforms in large discs such as

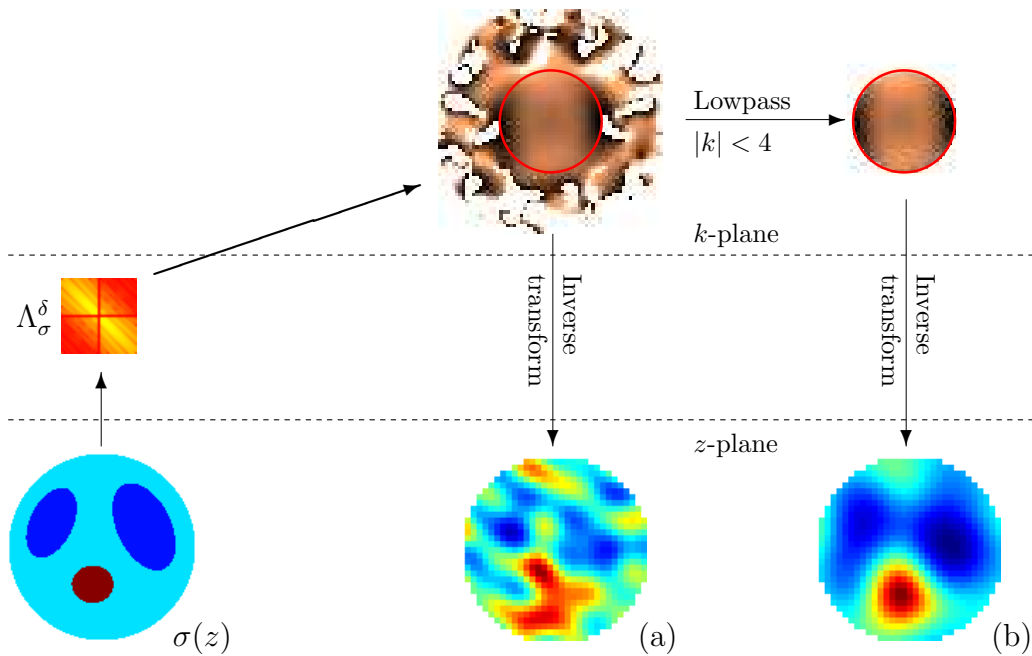


Figure 1: Schematic illustration of the nonlinear low-pass filtering approach to regularized EIT. This image corresponds to the so-called *shortcut method* defined below. The simulated heart-and-lungs phantom $\sigma(z)$ (bottom left) gives rise to a finite voltage-to-current matrix Λ_σ^δ (orange square), which can be used to determine the nonlinear Fourier transform. Measurement noise causes numerical instabilities in the transform (irregular white patches), leading to a bad reconstruction (a). However, multiplying the transform by the characteristic function of the disc $|k| < 4$ yields a lowpass-filtered transform, which in turn gives a noise-robust approximate reconstruction (b).

$|k| < 60$ and compute low-pass filtered reconstructions using inverse nonlinear Fourier transform and observe the results.

We compare two reconstruction methods based on the use of the CGO solutions (2.1): the *low-pass transport matrix method* implemented in [3], and a *shortcut method* based on solving a D-bar equation. The latter method does not have rigorous analysis available yet, but it is formally similar to the regularized EIT reconstruction algorithm studied in [43, 45, 40, 31, 30, 33, 34].

Our new computational findings can be roughly summarized by the following two points. First, both methods can approximate piecewise constant conductivities better and better as the cutoff frequency R increases, and there seems to be a Gibbs-like phenomenon producing ringing artifacts. Second, the transport matrix method loses accuracy away from a (freely chosen) pivot point located

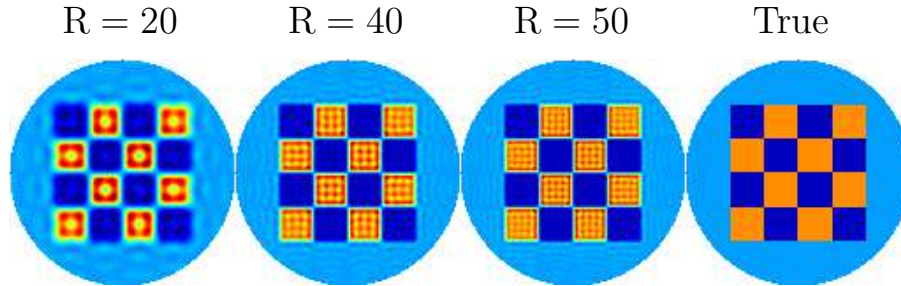


Figure 2: Convergence of nonlinearly low-pass filtered conductivity to the true discontinuous conductivity. Note the ringing artefacts reminiscent of the Gibbs effect of linear low-pass filtering. This picture illustrates the so-called shortcut method, and it is the first-ever computation of this kind with cutoff frequencies larger than 20.

outside of $\bar{\Omega}$, whereas the shortcut method produces reconstructions with more uniform quality.

Figure 2 shows some of our numerical results via the *shortcut method* for a nonsymmetric conductivity distribution.

The rotationally symmetric examples presented in Section 4.1 provide numerical evidence of the fact that discontinuous conductivities can be reconstructed with the shortcut method more and more accurately when R tends to infinity.

In the computational experiments we show in this paper, the truncated scattering transform is computed with a very large cutoff frequency through the Beltrami equation solver. In practice, it is not possible to obtain such scattering data from boundary measurements unless we had unrealistically high-precision EIT measurements available.

Notwithstanding the aforesaid, our new results are relevant for applications at least in these two ways:

- (1) We provide strong new evidence suggesting that the shortcut method can recover organ boundaries at the low-noise limit. Even with practical noise levels we can recover low-pass filtered jumps in the cases of nested inclusions or checkerboard-type discontinuity curves. While there are many dedicated methods for inclusion detection in EIT, for example [16, 9, 28, 8, 29, 25, 27, 39, 21, 17, 46, 22, 26, 23], none of them can locate nested inclusions.
- (2) The nonlinear Fourier transform studied here can be used to solve the nonlinear Noviko-Veselov (NV) equation. It is a nonlinear evolution equation generalizing the celebrated Korteweg-de Vries (KdV) equation into dimension $(2+1)$. There has been significant recent progress in linearizing

the NV equation using inverse scattering methods, see [38, 37, 44, 42, 14]. In the potential applications of the NV equation there should be no restriction to as low frequencies as in EIT.

We remark that all our numerical experiments have been computed using either a 192 Gigabyte computer with Linux or parallel computation provided by Techila.¹

2. THE NONLINEAR FOURIER TRANSFORM

In dimension two Calderón's problem [10] was solved using complex geometrical optics (CGO) solutions by Astala and Päivärinta [6]. In the case of L^∞ -conductivities σ the CGO solutions need to be constructed via the Beltrami equation

$$(2.1) \quad \bar{\partial}_z f_\mu = \mu \overline{\partial_z f_\mu}, \quad \text{with } f_\mu(z, k) = e^{ikz}(1 + \omega(z, k)),$$

where

$$\mu := \frac{1 - \sigma}{1 + \sigma}, \quad \omega(z, k) = \mathcal{O}\left(\frac{1}{z}\right) \text{ as } |z| \rightarrow \infty.$$

Here $z = z_1 + iz_2 \in \mathbb{C}$, $\bar{\partial}_z = (\partial/\partial z_1 + i\partial/\partial z_2)/2$ and k is a complex parameter.

More specifically, for $\sigma \in L^\infty(\mathbb{C})$ with $c^{-1} \leq \sigma(z) \leq c$ almost every $z \in \mathbb{C}$ and $\sigma \equiv 1$ outside the unit disc, and for $\kappa < 1$ with $|\mu(z)| \leq \kappa$ a.e. $z \in \mathbb{C}$, Theorem 4.2 in [6] establishes that for any $2 < p < 1 + 1/\kappa$ and complex parameter k , there exists a unique solution $f_\mu(\cdot, k)$ in the Sobolev space $W_{\text{loc}}^{1,p}(\mathbb{C})$ such that

$$(2.2) \quad \bar{\partial}_z f_\mu(z, k) = \mu(z) \overline{\partial_z f_\mu(z, k)}, \quad \text{for } z \in \mathbb{C},$$

holds with the asymptotic formula

$$(2.3) \quad f_\mu(z, k) = e^{ikz} \left(1 + \mathcal{O}\left(\frac{1}{z}\right) \right) \quad \text{as } |z| \rightarrow \infty.$$

In addition, $f_\mu(z, 0) \equiv 1$.

Write $f_{-\mu}$ for the solution to the Beltrami equation with coefficient $-\mu$. The scattering transform τ of Astala and Päivärinta (AP) is given by the formula

$$(2.4) \quad \overline{\tau(k)} = \frac{1}{2\pi} \int_{\mathbb{C}} \bar{\partial}_z (\omega(z, k) - \omega^-(z, k)) dz_1 dz_2,$$

where $\omega(z, k) := e^{-ikz} f_\mu(z, k) - 1$, $\omega^-(z, k) := e^{-ikz} f_{-\mu}(z, k) - 1$. It is known that $|\tau(k)| \leq 1$ for all $k \in \mathbb{C}$.

Defining the functions as follows for $k, z \in \mathbb{C}$:

$$(2.5) \quad h_+(z, k) := 1/2 (f_\mu(z, k) + f_{-\mu}(z, k)),$$

$$(2.6) \quad h_-(z, k) := i/2 (\overline{f_\mu(z, k)} - \overline{f_{-\mu}(z, k)}),$$

¹Techila Technologies Ltd is a privately held Finnish provider of High Performance Computing middleware solutions.

and

$$\begin{aligned} u_1(z, k) &:= h_+(z, k) - i h_-(z, k) = \operatorname{Re} f_\mu(z, k) + i \operatorname{Im} f_{-\mu}(z, k), \\ u_2(z, k) &:= i (h_+(z, k) + i h_-(z, k)) = -\operatorname{Im} f_\mu(z, k) + i \operatorname{Re} f_{-\mu}(z, k), \end{aligned}$$

it turns out that u_1, u_2 are the unique solutions to the following elliptic problems:

$$(2.7) \quad \nabla \cdot \sigma \nabla u_1 = 0, \quad u_1(z, k) = e^{ikz} (1 + \mathcal{O}(1/z)),$$

$$(2.8) \quad \nabla \cdot \sigma^{-1} \nabla u_2 = 0, \quad u_2(z, k) = e^{ikz} (i + \mathcal{O}(1/z)),$$

as $|z| \rightarrow \infty$.

The complex parameter k above can be understood as a nonlinear frequency-domain variable. As well as the function $\tau(k)$, defined in (2.4), plays the role of the nonlinear Fourier transform in the *shortcut method* described below, it is played by the following function

$$\nu_{z_0}(k) := i \frac{h_-(z_0, k)}{h_+(z_0, k)},$$

in the *low-pass transport matrix method* presented in Section 3.1, where z_0 is a pivot point outside $\bar{\Omega}$.

A practical algorithm was introduced in [5, 6, 3] for recovering σ approximately from a noisy measurement of Λ_σ . This algorithm involves a truncation operation (nonlinear low-pass filtering) in the frequency-domain.

The scattering transform used in [43] is defined as

$$(2.9) \quad \mathbf{t}(k) = \int_{\mathbb{R}^2} e^{i(kz + \bar{k}\bar{z})} q(z) m(z) dz,$$

where $q = \sigma^{-1/2} \Delta \sigma^{1/2}$ and σ is a strictly positive-real valued function in $W^{2,p}(\mathbb{R}^2)$ for some $p > 1$ with $\sigma \equiv 1$ on the unit disc near the boundary and outside the unit disc, and m solves the equation

$$m = 1 - g_k * (qm).$$

Here $*$ denotes convolution over the plane and g_k the Faddeev fundamental solution of $-\Delta - 4ik\bar{\partial}$. For smooth enough σ one can prove that

$$(2.10) \quad \mathbf{t}(k) = -4\pi i \bar{k} \tau(k).$$

In the rest of the paper, for non-smooth conductivities \mathbf{t} denotes the function defined through formula (2.10). Why are \mathbf{t} and τ called nonlinear Fourier transforms? There is admittedly some abuse of terminology involved, but the main reason is this. If one replaces m in (2.9) with 1, the result is the linear Fourier transform of q at $(-2k_1, 2k_2) \in \mathbb{R}^2$. But m is only asymptotically close to 1 and actually depends on q .

The following theorem holds:

Theorem 2.1. *Assume $\sigma \in L^\infty(\mathbb{R}^2)$ is real-valued, radially symmetric, bounded away from zero and $\sigma \equiv 1$ outside the unit disc. Then the function \mathbf{t} is real-valued and rotationally symmetric.*

Proof. The rotational symmetry of \mathbf{t} follows from the property $\mathbf{t}(k) = \mathbf{t}(\eta k)$ for any $\eta, k \in \mathbb{C}$ with $|\eta| = 1$, which is tantamount to $\tau(k) = \bar{\eta} \tau(\eta k)$. By uniqueness of the asymptotic boundary value problem (2.2)-(2.3), one can check that $f_\mu(z, \eta k) = f_\mu(\eta z, k)$. Therefore, $\omega(z, \eta k) = \omega(\eta z, k)$. For $-\mu$ the same equalities follow. Using definition (2.4) we deduce $\tau(k) = \bar{\eta} \tau(\eta k)$.

Thanks to $\mathbf{t}(k) = \mathbf{t}(\eta k)$, real-valuedness of \mathbf{t} follows from $\mathbf{t}(k) = \overline{\mathbf{t}(\bar{k})}$ and this fact is equivalent to seing $\tau(k) = \overline{\tau(-\bar{k})}$ due to the identity $\tau(\bar{k}) = \bar{\eta} \tau(\eta \bar{k})$ with $\eta = -1$. Again, by uniqueness of (2.2)-(2.3), it is straightforward to prove

$$f_\mu(z, k) = \overline{f_\mu(\bar{z}, -\bar{k})},$$

and $\omega(z, k) = \overline{\omega(\bar{z}, -\bar{k})}$. Attaining the same identity for $-\mu$ and by (2.4) we deduce $\tau(k) = \tau(-\bar{k})$. \square

3. INVERSE TRANSFORMS AND RECONSTRUCTION ALGORITHMS

3.1. The low-pass transport matrix method. Given noisy EIT data Λ_σ^δ , we can evaluate the traces of $M_\mu(\cdot, k) = 1 + \omega(\cdot, k)$ at the boundary $\partial\Omega$ for $|k| < R$ with some $R > 0$ depending on the noise level δ . This is achieved by the numerical method described in Section 4.1 of [3] based on solving the boundary integral equations studied in [5].

Once M_μ is known on the boundary, so is $f_\mu(\cdot, k)|_{\partial\Omega}$, which can be used to expand f_μ as a power series outside Ω . Choose a point $z_0 \in \mathbb{R}^2 \setminus \bar{\Omega}$. Set

$$(3.1) \quad \nu_{z_0}^{(R)}(k) := \begin{cases} i \frac{h_-(z_0, k)}{h_+(z_0, k)} & \text{for } |k| < R, \\ 0 & \text{for } |k| \geq R. \end{cases}$$

We next solve the truncated Beltrami equations

$$(3.2) \quad \bar{\partial}_k \alpha^{(R)} = \nu_{z_0}^{(R)}(k) \overline{\partial_k \alpha^{(R)}},$$

$$(3.3) \quad \bar{\partial}_k \beta^{(R)} = \nu_{z_0}^{(R)}(k) \overline{\partial_k \beta^{(R)}},$$

with solutions represented in the form

$$(3.4) \quad \alpha^{(R)}(z, z_0, k) = \exp(ik(z - z_0) + \varepsilon(k)),$$

$$(3.5) \quad \beta^{(R)}(z, z_0, k) = i \exp(ik(z - z_0) + \tilde{\varepsilon}(k)),$$

where $\varepsilon(k)/k \rightarrow 0$ and $\tilde{\varepsilon}(k)/k \rightarrow 0$ as $k \rightarrow \infty$. Requiring

$$(3.6) \quad \alpha^{(R)}(z, z_0, 0) = 1 \quad \text{and} \quad \beta^{(R)}(z, z_0, 0) = i$$

fixes the solutions uniquely.

To compute $\alpha^{(R)}$ we first find solutions η_1 and η_2 to the equation

$$(3.7) \quad \bar{\partial}_k \eta_j = \nu_{z_0}^{(R)}(k) \overline{\partial_k \eta_j},$$

with asymptotics

$$(3.8) \quad \eta_1(k) = e^{ik(z-z_0)}(1 + \mathcal{O}(1/k)),$$

$$(3.9) \quad \eta_2(k) = i e^{ik(z-z_0)}(1 + \mathcal{O}(1/k)),$$

respectively, as $|k| \rightarrow \infty$. There are constants $A, B \in \mathbb{R}$ such that $A\eta_1(0) + B\eta_2(0) = 1$. We now set $\alpha^{(R)}(z, z_0, k) = A\eta_1(k) + B\eta_2(k)$. Then $\alpha^{(R)}(z, z_0, k)$ satisfies the equation (3.2) and the appropriate asymptotic conditions.

Let $\alpha_{-\mu}^{(R)}$ denote the solution to (3.2) with the condition (3.4) so that the coefficient $\nu_{z_0}^{(R)}$ is computed interchanging the roles of μ and $-\mu$. Then $\beta_{\mu}^{(R)} = i\alpha_{-\mu}^{(R)}$. For computational construction of the frequency-domain CGO solutions η_j satisfying (3.7–3.9), see [3, Section 5.2] and [24].

Fix any nonzero $k_0 \in \mathbb{C}$ and choose any point z inside the unit disc. Denote $\alpha^{(R)} = a_1^{(R)} + ia_2^{(R)}$ and $\beta^{(R)} = b_1^{(R)} + ib_2^{(R)}$. We can now use the truncated transport matrix

$$(3.10) \quad T^{(R)} = T_{z, z_0, k_0}^{(R)} := \begin{pmatrix} a_1^{(R)} & a_2^{(R)} \\ b_1^{(R)} & b_2^{(R)} \end{pmatrix}$$

to compute

$$(3.11) \quad \begin{aligned} u_1^{(R)}(z, k_0) &= a_1^{(R)}u_1(z_0, k_0) + a_2^{(R)}u_2(z_0, k_0), \\ u_2^{(R)}(z, k_0) &= b_1^{(R)}u_1(z_0, k_0) + b_2^{(R)}u_2(z_0, k_0). \end{aligned}$$

We know the approximate solutions $u_j^{(R)}(z, k_0)$ for $z \in \Omega$ and one fixed k_0 . We use formulas $u_1^{(R)} = h_+^{(R)} - ih_-^{(R)}$, $u_2^{(R)} = i(h_+^{(R)} + ih_-^{(R)})$ and (2.5)-(2.6) (with $z \in \Omega$) to connect $u_1^{(R)}, u_2^{(R)}$ with $f_{\mu}^{(R)}, f_{-\mu}^{(R)}$. Define

$$(3.12) \quad \mu^{(R)}(z) = \frac{\bar{\partial} f_{\mu}^{(R)}(z, k_0)}{\partial f_{\mu}^{(R)}(z, k_0)}.$$

Finally we reconstruct the conductivity σ approximately as

$$(3.13) \quad \sigma^{(R)} = \frac{1 - \mu^{(R)}}{1 + \mu^{(R)}}.$$

3.2. The shortcut method. Fix $R > 0$ corresponding to a certain noise level δ in the EIT data. For all $|k| < R$, we compute the traces of $M_{\mu}(\cdot, k)$ and $M_{-\mu}(\cdot, k)$ by solving the boundary integral equation aforementioned in Section 3.1. The analyticity of $M_{\mu}(\cdot, k)$, $M_{-\mu}(\cdot, k)$ outside the unit disc allows to develop these factors as follows

$$M_{\mu}(z, k) = 1 + \frac{a_1^+(k)}{z} + \frac{a_2^+(k)}{z^2} + \dots, \quad M_{-\mu}(z, k) = 1 + \frac{a_1^-(k)}{z} + \frac{a_2^-(k)}{z^2} + \dots,$$

for $|z| > 1$.

In Section 5 of [6] it is proved that the scattering transform τ satisfies

$$\tau(k) = \frac{1}{2} (\overline{a_1^+(k)} - \overline{a_1^-(k)}), \quad k \in \mathbb{C}.$$

Notice that this formula is consistent with (2.4). Let $\tau_R^\delta(k)$ be a numerical approximation to $\tau(k)$ such that $\tau_R^\delta(k) = 0$ for $|k| > R$.

For all $z \in \Omega$, we solve the D-bar equation

$$(3.14) \quad \bar{\partial}_k m_R^\delta(z, k) = -i \tau_R^\delta(k) e_{-z}(k) \overline{m_R^\delta(z, k)}$$

with $m_R^\delta(z, \cdot) - 1 \in L^r(\mathbb{R}^2) \cap L^\infty(\mathbb{R}^2)$, for some $r > 2$.

Finally, we reconstruct σ approximately as $\sigma(z) \approx (m_R^\delta(z, 0))^2$. This method is proven to work for C^2 conductivities σ by computing the approximation $\tau_R^\delta(k)$ in a different way, namely the methods described in [43, 45, 40, 31, 30, 33, 34]. Nevertheless, there is no theoretical understanding of what happens when σ is nonsmooth and only essentially bounded.

3.3. Periodization of the nonlinear inverse transform. The algorithm we use to solve equation (3.14) is presented in [35] and is a modification of the method introduced by Vainikko in [47] for the Lippmann-Schwinger equation related to the Helmholtz equation. Such algorithm is based in reducing the equation

$$(3.15) \quad m_R(z, k) = 1 + \frac{1}{\pi} \int_{B_R} \frac{F(z, k') \overline{m_R(z, k')}}{k - k'} dk',$$

to a periodic one. Let us see how this reduction is done.

Here $F(z, k) := -i \tau(k) e_{-k}(z)$ and $e_k(z) := e^{ikz + i\bar{k}\bar{z}}$.

Take $\epsilon > 0$ and set $s = 2R + 3\epsilon$. Define $Q = [-s, s]^2$. Choose an infinitely smooth cutoff function $\eta \in C_0^\infty(\mathbb{R}^2)$ verifying

$$\eta(k) = \begin{cases} 1 & \text{for } |k| < 2R + \epsilon, \\ 0 & \text{for } |k| \geq 2R + 2\epsilon, \end{cases}$$

and $0 \leq \eta(k) \leq 1$ for all $k \in \mathbb{C}$.

Definition 3.1. We say a function f defined on the plane is $2s$ -periodic if $f(k) = f(k + 2s(j_1 + ij_2))$ for any $k \in \mathbb{C}$, $j_1, j_2 \in \mathbb{Z}$. That is to say, we mean that f is $2s$ -periodic in each coordinate.

Notation. $L^p(Q)$ denotes the space of $2s$ -periodic functions in $L_{loc}^p(\mathbb{R}^2)$ for $1 \leq p \leq \infty$. Note that $L^\infty(Q) \subset L^\infty(\mathbb{R}^2)$.

For any measurable subset A of \mathbb{R}^2 we denote by χ_A both the characteristic function of A and the multiplier operator with such function in k .

We write \mathcal{E}_0 to denote the extension by zero outside the torus Q defined as

$$\mathcal{E}_0 f(z, k) = \begin{cases} f(z, k), & \text{if } k \in Q, \\ 0, & \text{if } k \in \mathbb{C} \setminus Q, \end{cases}$$

for any $f(z, \cdot) \in L^1(Q)$.

Define a $2s$ -periodic approximation to the principal value $1/(\pi k)$ by setting $\tilde{\beta}(k) = \eta(k)/(\pi k)$ for $k \in Q$ and extending periodically:

$$\tilde{\beta}(k + 2j_1s + i2j_2s) = \frac{\eta(k)}{\pi k} \quad \text{for } k \in Q, j_1, j_2 \in \mathbb{Z}.$$

Define a periodic approximate solid Cauchy transform in k by

$$\tilde{\mathcal{C}}_0 f(z, k) = (\tilde{\beta} * f)(z, k) = \int_Q \tilde{\beta}(k - k') f(z, k') dk',$$

where $\tilde{*}$ denotes convolution on the torus.

We shall use another periodization of the Cauchy transform given by

$$\tilde{\mathcal{C}} f(z, k) = \mathcal{E} \chi_{\mathbb{D}_{R+c}} \tilde{\mathcal{C}}_0 f(z, k),$$

where \mathcal{E} denotes the periodic extension operator defined as

$$\mathcal{E} f(z, k + 2s(j_1 + ij_2)) = f(z, k), \quad \text{for any } k \in Q, j_1, j_2 \in \mathbb{Z}.$$

Define the multiplication operator F_R by $F_R f(z, k) = \chi_{B_R}(k) F(z, k) f(z, k)$ if $k \in \mathbb{C}$ and its periodization as

$$\tilde{F}_R f(z, k + 2j_1s + i2j_2s) = F_R f(z, k), \quad \text{for } j_1, j_2 \in \mathbb{Z}, k \in Q.$$

Let us denote the complex conjugation operator by \mathbf{c} , i.e. $\mathbf{c}(f) = \bar{f}$. We periodize the complex conjugation operator $\tilde{\mathbf{c}}$ in the same way.

We shall need some boundedness properties of the so-called Cauchy transform. The Cauchy transform, we denote it by $\bar{\partial}^{-1}$, is defined as the following weakly singular integral operator:

$$\bar{\partial}^{-1} f(k) = \frac{1}{\pi} \int_{\mathbb{R}^2} \frac{f(k')}{k - k'} dk'_1 dk'_2,$$

where $k' = k'_1 + ik'_2$ and $dk'_1 dk'_2$ denotes the Lebesgue measure on \mathbb{R}^2 .

Theorem 4.3.8 in [2] states that

$$(3.16) \quad \left\| \bar{\partial}^{-1} \phi \right\|_{L^{q^*}(\mathbb{C})} \leq \frac{C}{(q-1)(2-q)} \|\phi\|_{L^q(\mathbb{C})}$$

for some constant C , $1 < q < 2$ and $q^* = 2q/(2-q)$.

For any $1 < q < \infty$ and $1/q + 1/q' = 1$ the space $L^q(\mathbb{C}) \cap L^{q'}(\mathbb{C})$ with the norm $\|\cdot\|_{L^q} + \|\cdot\|_{L^{q'}}$ is a Banach space. Theorem 4.3.11 in [2] claims the following:

Theorem 3.1. *When $1 < q < 2$ the Cauchy transform maps continuously the space $L^q(\mathbb{C}) \cap L^{q'}(\mathbb{C})$ into the space of continuous functions on the plane vanishing at infinity with the sup norm and satisfies the estimate*

$$\left\| \bar{\partial}^{-1} \phi \right\|_{L^\infty(\mathbb{C})} \leq (2-q)^{-1/2} (\|\phi\|_{L^q(\mathbb{C})} + \|\phi\|_{L^{q'}(\mathbb{C})}).$$

It is easy to see that if $1 < q_1 < 2 < q_2 < \infty$ but not necessarily $q_1^{-1} + q_2^{-1} = 1$ then

$$(3.17) \quad \left\| \bar{\partial}^{-1} \phi \right\|_{L^\infty(\mathbb{C})} \lesssim \left(\|\phi\|_{L^{q_1}(\mathbb{C})} + \|\phi\|_{L^{q_2}(\mathbb{C})} \right),$$

and $\bar{\partial}^{-1} \phi$ is a continuous function assuming the right hand side bounded, where the implicit constant just depends on q_1, q_2 .

We conclude this section with the Theorem 3.2. Its proof uses the aforementioned properties of the Cauchy transform and is quite similar to the arguments presented in Sections 14.3.3 and 15.4.1 of the book [41]. Some of the techniques for Theorem 4.1 in [43] are involved.

Theorem 3.2. *Assume $c^{-1} \leq \sigma \leq c$ a.e. in the plane and $\sigma \equiv 1$ outside the unit disc. Let $z \in \mathbb{C}$. There exists a unique $2s$ -periodic (in k) solution $\tilde{m}_R(z, k)$ to*

$$(3.18) \quad \tilde{m}_R(z, k) = 1 + \tilde{\mathcal{C}} \tilde{F}_R \tilde{\mathcal{C}} \tilde{m}_R(z, k), \quad \text{a.e. } k \in Q,$$

with $\tilde{m}_R(z, \cdot) \in L^r(Q)$ for some $2 < r < \infty$.

Furthermore, the solutions of (3.15) and (3.18) agree on the disc of the k -plane with radius R : $m_R(z, k) = \tilde{m}_R(z, k)$ for $|k| < R$.

4. COMPUTATIONAL RESULTS

Once scattering data with big cutoff frequencies are generated, we test the non-linear inversion procedure consisting of computing the approximate conductivity from the truncated scattering transform by solving

$$(4.1) \quad \bar{\partial}_k m_R(z, k) = \chi_{B_R}(k) (-i) \tau(k) e_{-k}(z) \overline{m_R(z, k)},$$

with

$$(4.2) \quad m_R(z, \cdot) - 1 \in L^\infty(\mathbb{R}^2) \cap L^{r_0}(\mathbb{R}^2), \quad \text{for some } r_0 \in (2, \infty).$$

The unique solution $m_R(z, k)$ to (4.1) with the normalization condition (4.2) can be obtained by solving (3.15). Finally, the approximate reconstruction $\tilde{\sigma}_R(z)$ is obtained by doing $\tilde{\sigma}_R(z) := m_R(z, 0)^2$ for $|z| < 1$.

4.1. Nonlinear Gibbs phenomenon in radial cases. In this section we test the shortcut method for two radially symmetric conductivities as follows: Firstly, we solve numerically the Beltrami equation and obtain reliable scattering data over a mesh for a real interval of the form $[0, R]$ with $R > 0$. Secondly, from such scattering data the approximate reconstruction is computed by solving numerically the equation (3.18) on a mesh for the real interval $[0, 1]$. It suffices to confine such computations to real positive numbers since the results on the whole disc can be obtained by simple rotation with respect to the origin by symmetry. The pictures for such reconstructions corresponding to the largest cutoff frequencies exhibit certain artifacts near the jump discontinuities of the actual conductivity quite similar to the Gibbs phenomenon for the truncated linear Fourier transform.

4.1.1. *Example σ_1 .* We consider the rotationally symmetric conductivity σ_1 on the plane defined as $\sigma_1(z) = 2$ if $|z| < 0.5$ and $\sigma_1(z) = 1$ if $|z| \geq 0.5$. Figure 3 shows its representation.

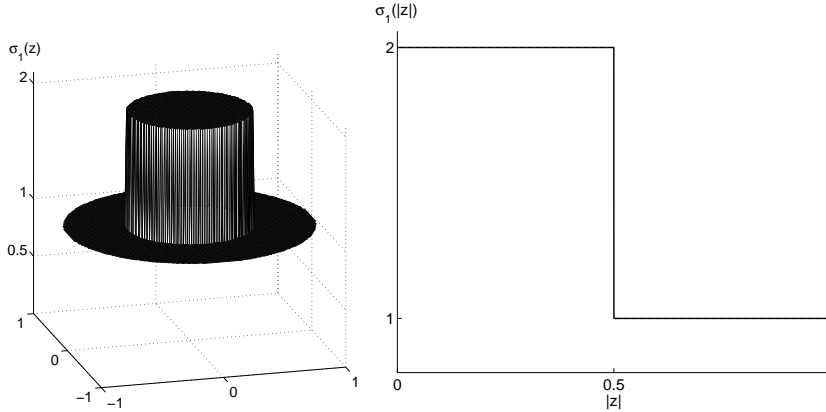


Figure 3: Rotationally symmetric conductivity example σ_1 . Left: plot of σ_1 as a function of z ranging in the unit disc with jump discontinuities along the curve $|z| = 0.5$. Right: Profile of σ_1 as a function of $|z|$ ranging in $[0,1]$ with a jump discontinuity at $|z| = 0.5$.

Computing the scattering transform

The numerical evaluation of the AP scattering transform $\tau(k)$ was computed for this example conductivity σ_1 . The used algorithm generates for each fixed k CGO solutions for the Beltrami equation in the z -plane using the Huhtanen-Perämäki preconditioned solver ([24]) by executing standard \mathbb{C} -linear GMRES. To do so a z -grid is required. Such a z -grid is determined by a size parameter m_z so that $2^{m_z} \times 2^{m_z}$ equidistributed points are taken in the z -plane within the square $[-s_z, s_z) \times [-s_z, s_z)$ with $s_z = 2.1$ and step $h_z = s_z/2^{m_z-1}$. Let us denote the numerical computation of τ with a z -grid size parameter m_z by $\tilde{\tau}_{m_z}$.

We know that for radial, real-valued conductivities the function \mathbf{t} is rotationally symmetric too (Theorem 2.1). Therefore, we can restrict the numerical computation of \mathbf{t} to positive values of the k -plane. The chosen k -grid was all the points in the interval $[0, 150]$ with step $h = 0.1$. Thus, the scattering transform is computed farther away from the origin than any previous computation.

The vector $\tilde{\tau}_{m_z}$ corresponding to the aforementioned k -grid was computed for both $m_z = 10$ and $m_z = 11$. Next, the function $\tilde{\mathbf{t}}_{m_z}$ defined as

$$\tilde{\mathbf{t}}_{m_z}(k) = -4\pi i \bar{k} \tilde{\tau}_{m_z}(k),$$

was evaluated on the same k -grid in $[0, 150]$ for $m_z = 10, 11$ from the AP scattering transform using identity (2.10).

One can consider the approximate scattering transform $\tilde{\tau}_{11}$ (with $m_z = 11$) reliable since its accuracy is high in a double sense.

On one hand, Figure 4 shows the lack of significant differences between $\tilde{\mathbf{t}}_{10}$ and $\tilde{\mathbf{t}}_{11}$ for k close to the origin. As a matter of fact, using the notation

$$(4.3) \quad E_B := \frac{\max_{|k| \in B} |\operatorname{Im}(\tilde{\tau}_{10}(k) - \tilde{\tau}_{11}(k))|}{\max_{|k| \in B} |\operatorname{Im}(\tilde{\tau}_{11}(k))|} \cdot 100\%$$

for a subinterval B of $[0, 150]$, it follows that

$$E_{[0,20]} = 0.3533\%, \quad E_{[20,40]} = 4.0258\%, \quad E_{[40,60]} = 9.8138\%.$$

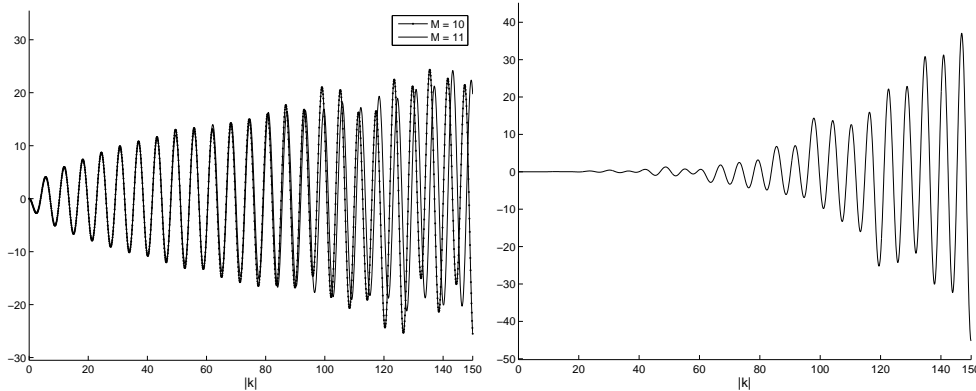


Figure 4: Comparison between $\tilde{\mathbf{t}}_{10}$ and $\tilde{\mathbf{t}}_{11}$ for σ_1 . Left: Profiles of the real parts of $\tilde{\mathbf{t}}_{10}$ (thin dotted line) and $\tilde{\mathbf{t}}_{11}$ (thick solid line). Right: Profile of the difference $\operatorname{Re}(\tilde{\mathbf{t}}_{10} - \tilde{\mathbf{t}}_{11})$. In both pictures $|k|$ ranges in $[0, 150]$ with step $h = 0.1$.

On the other hand, $|\operatorname{Re}(\tilde{\tau}_{11})|$ is very small. By Theorem 2.1 and formula (2.10), for a rotationally symmetric, real-valued conductivity the scattering transform τ restricted to real numbers has to be pure-imaginary valued. We obtain a nonzero real part $\operatorname{Re}(\tilde{\tau}_{m_z})$ for both m_z values due to precision errors. In particular,

$$|\operatorname{Re}(\tilde{\tau}_{11})| \leq 3.7196 \times 10^{-9}.$$

Note that one can extend $\tilde{\mathbf{t}}_{11}$ to the disc centered at the origin with radius 150 in the k -plane by simple rotation since $\tilde{\mathbf{t}}_{11}(k_1) = \tilde{\mathbf{t}}_{11}(k_2)$ if $|k_1| = |k_2|$.

Solving the D-bar equation

We compute a number of reconstructions of σ_1 using the D-bar method truncating the approximate scattering transform $\tilde{\tau}_{11}$. This way the computation is optimized by restricting the degrees of freedom to the values of $\tilde{\tau}_{11}(k)$ at grid points satisfying $|k| < R$, for some positive number R called the cutoff frequency.

The program constructs the set of evaluation points in the k -plane for which the D-bar equation is solved for every fixed z , as a k -grid of $2^{m_k} \times 2^{m_k}$ points

within the square $[-s_k, s_k) \times [-s_k, s_k)$ with $s_k = 2.3 \times R$ and step $h_k = s_k/2^{m_k-1}$. Let $\tilde{\sigma}_1(z; m_k, R)$ denote the shortcut reconstruction of σ_1 with size parameter m_k and truncation radius R .

Again we can restrict the computation (of $\tilde{\sigma}_1(z; m_k, R)$ in this case) to positive values in the z -domain and afterwards extend to the plane by rotation. We evaluated $\tilde{\sigma}_1(z; m_k, R)$ for each point z in a grid of a certain number N_x of equispaced points in the real interval $[0,1]$.

The vector $\tilde{\sigma}_1(z; m_k, R)$ was computed for $R = 5, 10, 15, 20, 25, 30, 35, 40, 50, \dots, 150$. For $R = 5, 10$ we took $m_k = 8, 9$ and for the rest of R values we chose $m_k = 12$. These are by far the largest nonlinear cut-off frequencies studied numerically so far. In Figure 5 the reader can see three of these reconstruction examples.

Since the shortcut reconstruction for σ_1 is real-valued, the obtained imaginary parts are due to precision errors. Such errors are displayed multiplied by 10^8 in the following tables:

m_k	8	8	9	9	12	12	12	12	12	12	12	12	12	12
R	5	10	5	10	15	20	25	30	35	40	50	60	70	80
$\mathbf{error}_1 \times 10^8$	4.67	2.36	4.67	2.36	2.15	2.24	2.57	2.84	3.04	3.26	3.55	3.78	4	4.19

m_k	12	12	12	12	12	12	12
R	90	100	110	120	130	140	150
$\mathbf{error}_1 \times 10^8$	4.36	4.48	4.57	4.61	4.62	4.76	4.89

where $\mathbf{error}_1 = \max_{|z| \leq 1} |\text{Im}(\tilde{\sigma}_1(z; m_k, R))|$.

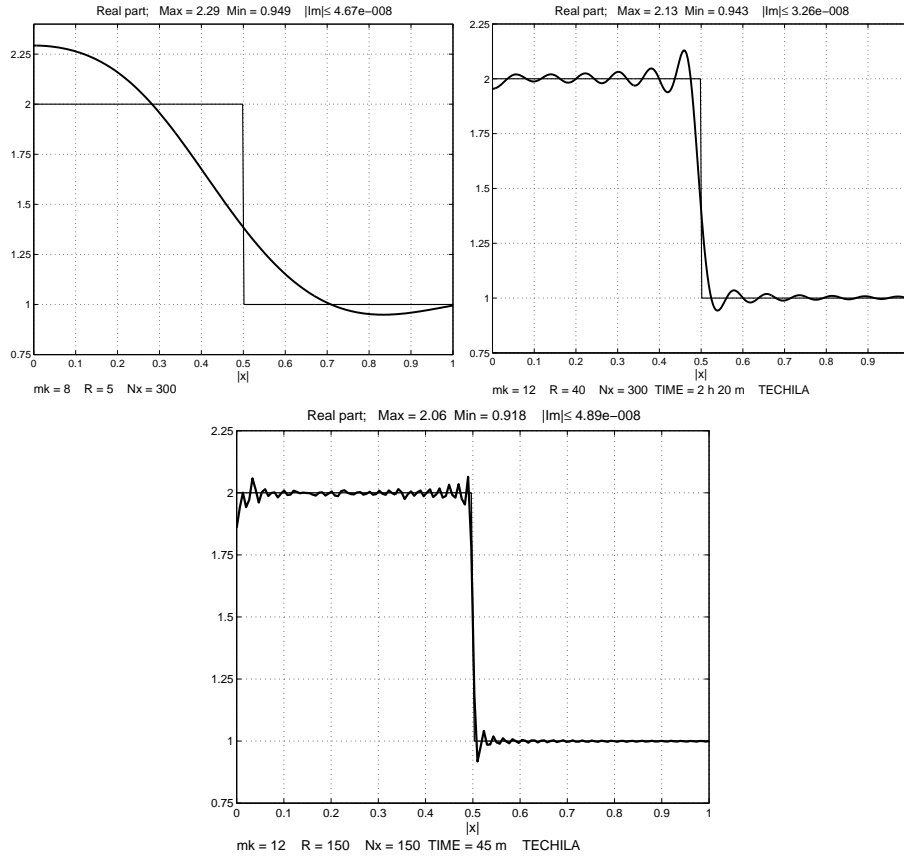


Figure 5: Three shortcut method reconstruction examples computed from a scattering transform corresponding to σ_1 . Each picture shows the real part of the approximate reconstruction (thick line) and the original conductivity σ_1 (thin line). In addition, the following information is shown: maximum and minimum values of the real part of the reconstruction, maximum of the absolute value of the imaginary part of the reconstruction (error), taken parameters m_k , R , N_x and computation time if possible. The examples for $m_k = 12$ and $R = 40, 150$ were computed using grid computation provided by Techila.

4.1.2. *Example σ_2 .* Now, we repeat the same experiments for another rotationally symmetric conductivity example σ_2 defined as follows: $\sigma_2(z) = 2$ if $|z| < 0.1$, $0.2 < |z| < 0.3$ or $0.4 < |z| < 0.5$ and $\sigma_2(z) = 1$ otherwise. Figure 6 shows its profiles.

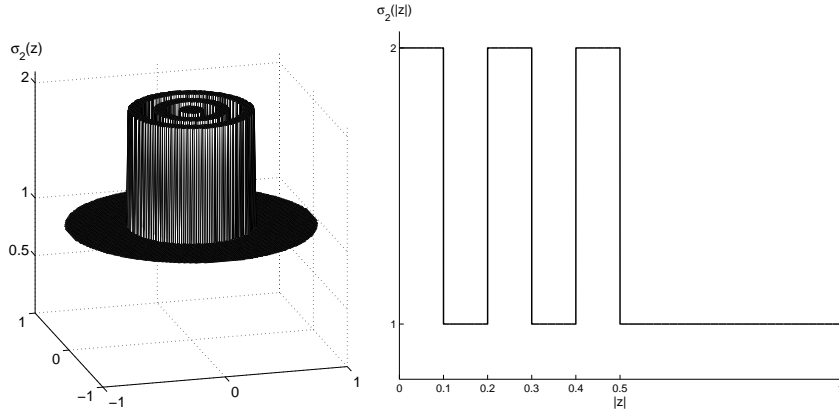


Figure 6: Rotationally symmetric conductivity example σ_2 . Left: plot of σ_2 as a function of z ranging in the unit disc with jump discontinuities along the curves $|z| = 0.1, |z| = 0.2, |z| = 0.3, |z| = 0.4, |z| = 0.5$. Right: Profile of σ_2 as a function of $|z|$ ranging in $[0,1]$ with jump discontinuities at $|z| = 0.1, |z| = 0.2, |z| = 0.3, |z| = 0.4, |z| = 0.5$.

Computing the scattering transform

For conductivity σ_2 the scattering transform $\tilde{\tau}_{11}$ (with $m_z = 11$) turns out to be very accurate too. Indeed, $\tilde{\mathbf{t}}_{10}$ and $\tilde{\mathbf{t}}_{11}$ corresponding to σ_2 are quite similar for $|k|$ small in view of Figure 7 and the following facts (see notation (4.3)):

$$E_{[0,20]} = 0.4606\%, \quad E_{[20,40]} = 3.7474\%, \quad E_{[40,60]} = 6.4308\%, \quad \text{for } \sigma_2,$$

$$|\text{Re}(\tilde{\tau}_{11})| \leq 1.3653 \times 10^{-7}, \quad \text{for } \sigma_2.$$

Solving the D-bar equation

Likewise the vector $\tilde{\sigma}_2(z; m_k, R)$ was computed for $R = 5, 10, 15, 20, 25, 30, 35, 40, 50, \dots, 150$. For $R = 5, 10$ we took $m_k = 8, 9$ and for the rest of R values we chose $m_k = 12$. All these reconstructions were computed using parallel computation provided by Techila. Figure 8 shows some of these numerical results. Below we list the errors $\text{error}_2 = \max_{|z| \leq 1} |\text{Im}(\tilde{\sigma}_2(z; m_k, R))|$:

m_k	8	8	9	9	12	12	12	12	12	12	12	12	12	12
R	5	10	5	10	15	20	25	30	35	40	50	60	70	80
$\text{error}_2 \times 10^7$	1.56	2.16	1.56	2.17	5.12	5.65	3.97	4.88	6.48	14.1	19.3	14.8	18.4	28.4
m_k	12	12	12	12	12	12	12							
R	90	100	110	120	130	140	150							
$\text{error}_2 \times 10^7$	20.3	20.7	28.8	25.3	24.3	21.8	19.7							

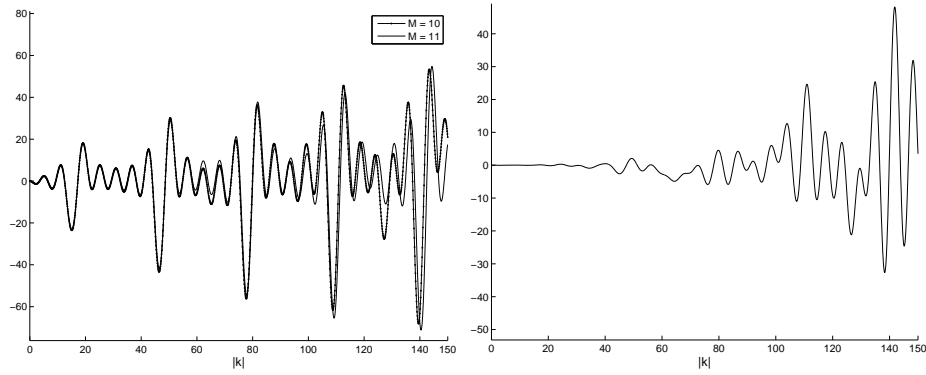


Figure 7: Comparison between $\tilde{\mathbf{t}}_{10}$ and $\tilde{\mathbf{t}}_{11}$ for σ_2 . Left: Profiles of the real parts of $\tilde{\mathbf{t}}_{10}$ (thin dotted line) and $\tilde{\mathbf{t}}_{11}$ (thick solid line). Right: Profile of the difference $\text{Re}(\tilde{\mathbf{t}}_{10} - \tilde{\mathbf{t}}_{11})$. In both pictures $|k|$ ranges in $[0, 150]$ with step $h = 0.1$. Note that the vertical axis scales are different from Figure 4.

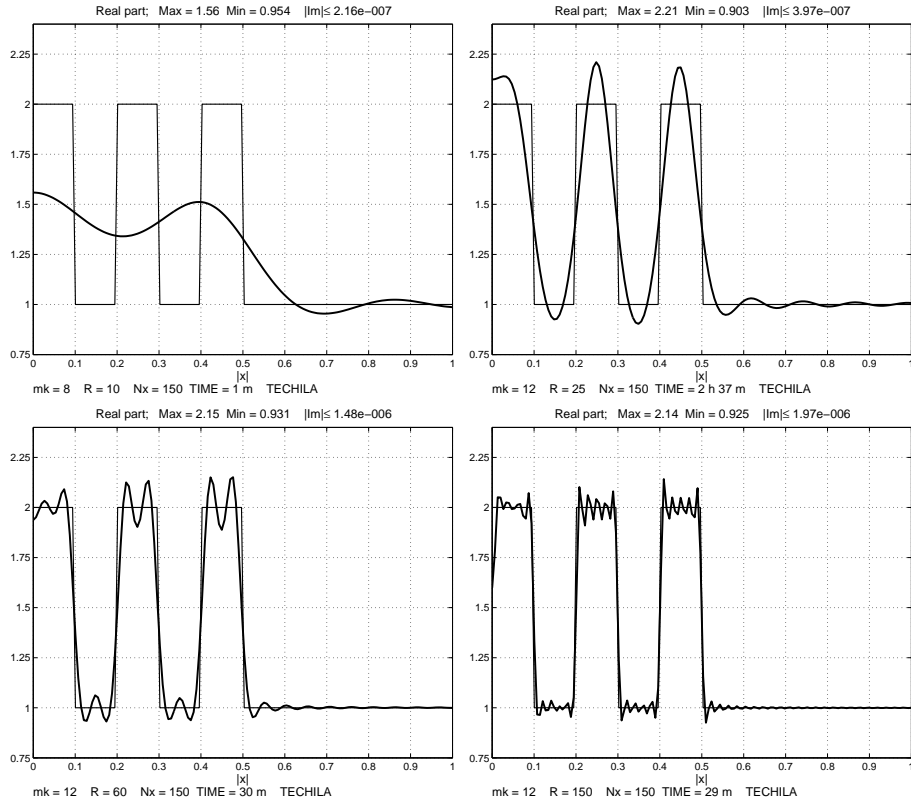


Figure 8: Four shortcut method reconstruction examples computed from a scattering transform corresponding to σ_2 . Each picture shows the real part of the approximate reconstruction (thick line) and the original conductivity σ_2 (thin line). In addition, the following information is shown: maximum and minimum values of the real part of the reconstruction, maximum of the absolute value of the imaginary part of the reconstruction (error), taken parameters m_k , R , N_x and computation time. Axes scale is the same in the four profiles. These examples were computed using grid computation provided by Techila.

4.2. Comparison of the two methods in nonsymmetric cases. We apply both reconstruction methods to some discontinuous non-radial “checkerboard-style” conductivities without assuming EIT data. We choose the conductivity examples σ_3 , σ_4 shown in Figure 9. Both take value 1 near the boundary of the unit disc. Notice that the contrasts of these examples σ_3 , σ_4 (defined as the difference between the maximum and the minimum) are 1.5 and 2.8, respectively.

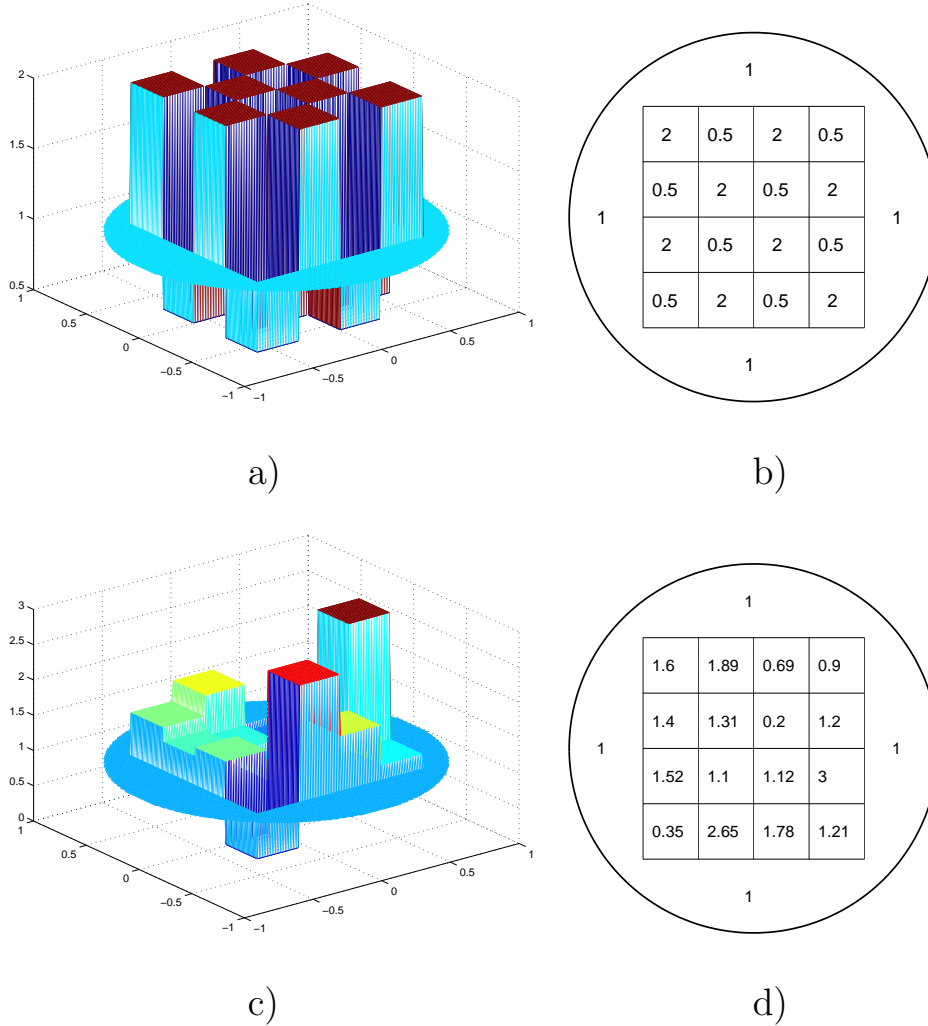


Figure 9: Checkerboard style conductivities σ_3 , σ_4 : a), c) show the picture for σ_3 , σ_4 , resp., using mesh Matlab function. b), d) show the values for σ_3 , σ_4 , resp., over each tile.

Figures 12, 13 show the approximate reconstructions for both examples and certain cut-off frequencies R using both methods. The relative errors with sup and l^2 norms over the matrix of chosen points in the unit disc are pointed out. We denote such errors as follows:

$$\text{sup} = \frac{\|\sigma - \tilde{\sigma}\|_{l^\infty}}{\|\sigma\|_{l^\infty}} \cdot 100 \%, \quad \text{sqr} = \frac{\|\sigma - \tilde{\sigma}\|_{l^2}}{\|\sigma\|_{l^2}} \cdot 100 \%,$$

where σ denotes the actual conductivity and $\tilde{\sigma}$ the approximate reconstruction.

Low-pass transport matrix method

In order to test the low-pass transport matrix method for each conductivity, we obtain the CGO solutions $f_\mu(z_0, k)$, $f_{-\mu}(z_0, k)$ directly from the known conductivities without simulating EIT data. The point z_0 is outside the unit disc and we take the k -grid of $2^{m_k} \times 2^{m_k}$ equispaced points in the square $[-R, R]^2$ with step $h_k = R/2^{m_k-1}$ and cut-off frequencies $R \leq 50$. Next, transportation of $f_\mu(z_0, k)$, $f_{-\mu}(z_0, k)$ to the unit disc and the final reconstruction $\sigma^{(R)}$ are performed following the steps described in Section 3.1. To this end, in addition to the k -grid, a grid in the z -variable of $2^{m_z} \times 2^{m_z}$ equidistributed points in the square $[-s_z, s_z]^2$, with step $h_z = s_z/2^{m_z-1}$, is required.

For σ_3, σ_4 we choose $z_0 = (-0.88594, -0.88594)$, $z_0 = (0, 1.2656)$, respectively. For σ_3 we take $m_z = 7$, $m_k = 8$ and for σ_4 $m_z = 7$, $m_k = 7$. The reconstructions of σ_3 could be computed for $R \leq 50$ but not for σ_4 with $R > 20$.

Shortcut method

Concerning the shortcut method, firstly the approximate scattering transform, denote it by τ_j^{SC} for σ_j ($j = 3, 4$), is computed directly from the known conductivity through the Beltrami equation solver using formula (2.4). The code evaluates the approximation over the points inside the disc of radius R (cut-off frequency) from a k -grid of $2^{m_k} \times 2^{m_k}$ equispaced points in the square $[-R, R]^2$. Another z -grid with $2^{m_z} \times 2^{m_z}$ points in $[-s_z, s_z]^2$ ($s_z > 2$) is involved here.

To compute τ_3^{SC} we take $R = 50$, $m_k = 8$, $m_z = 10$, and for τ_4^{SC} we choose $R = 50$, $m_k = 7$, $m_z = 7$. Let us remark that this choice of R enables reconstructions corresponding to cut-off frequencies less than or equal to 50.

Secondly, Figures 10, 11 show plots of τ_j^{SC} and \mathbf{t}_j^{SC} , where $j = 3, 4$ and \mathbf{t}_j^{SC} is computed from τ_j^{SC} by formula (2.10).

Finally, we evaluate the approximate reconstruction by solving the D-bar equation with the truncated scattering transform τ_j^{SC} as a coefficient. The reconstructions are computed over the points of the same kind of z -grid as above belonging to the unit disc with size parameter m_z . The code computes the solution to the D-bar equation on every point in the z -grid independently and uses a number of k -grids with size parameter m_k and cut-off frequency R .

These reconstructions were evaluated with $m_z = 7$ and some R values with $R \leq 50$. In addition, with respect to σ_3 we took $m_k = 9$ and for σ_4 , $m_k = 7$.

Notice that the case $R = 50$ was correctly computed for both conductivities σ_3 , σ_4 using the shortcut method, but for σ_4 the highest R -value through the low-pass transport matrix method was $R = 20$.

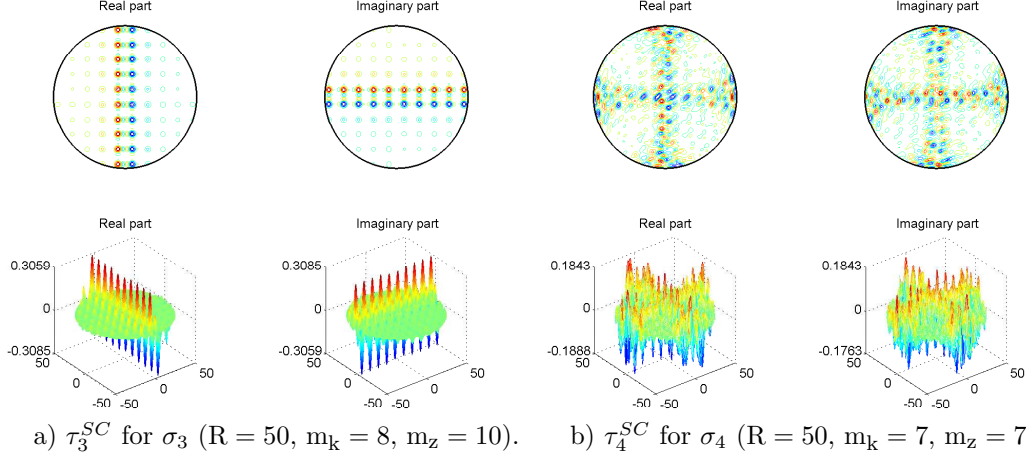


Figure 10: a) Plot of real (left) and imaginary (right) parts of the scattering transform τ_3^{SC} for the conductivity example σ_3 . b) Idem for τ_4^{SC} corresponding to σ_4 .

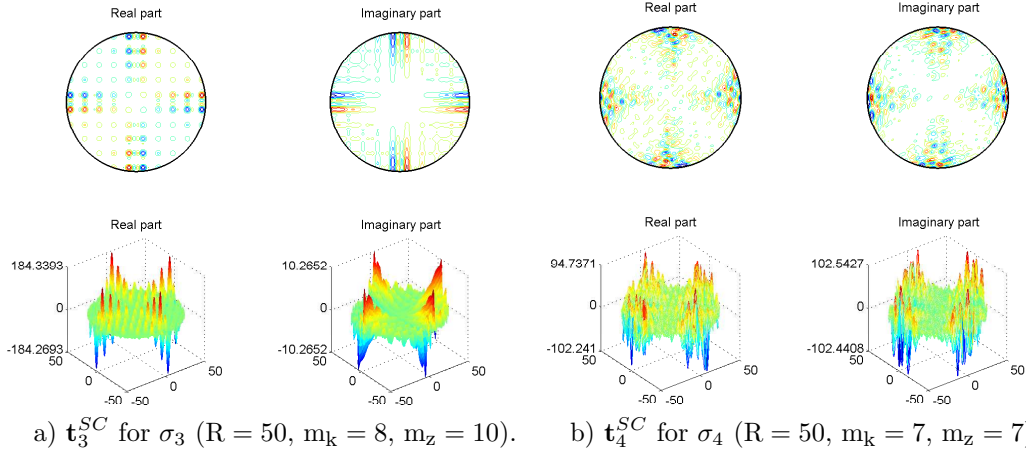


Figure 11: a) Plot of real (left) and imaginary (right) parts of the scattering transform t_3^{SC} for the conductivity example σ_3 . b) Idem for t_4^{SC} corresponding to σ_4 .

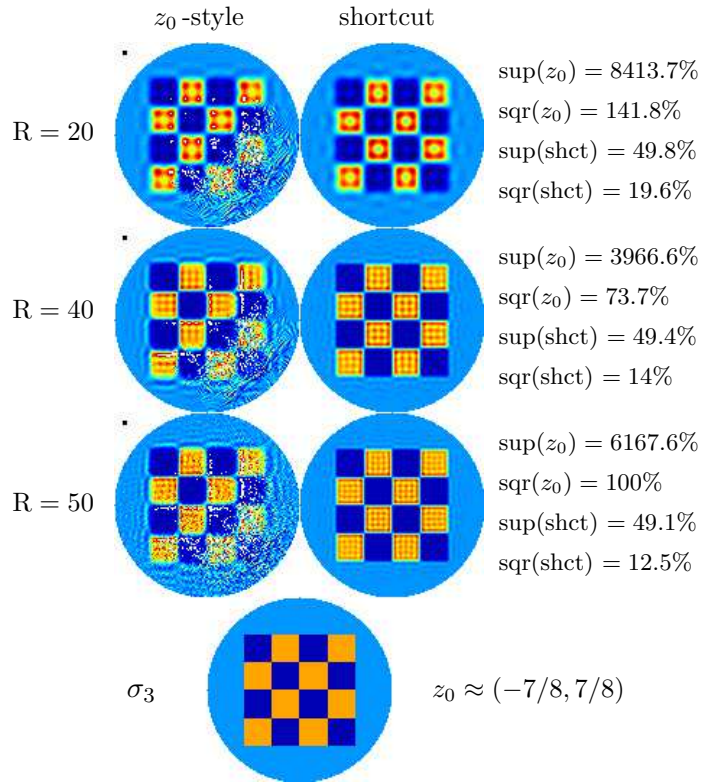


Figure 12: Comparison of reconstructions for σ_3 by the low-pass transport matrix method (left) and the shortcut method (right) using different cut-off frequencies R . The chosen point z_0 appears in black. The true conductivity is represented at the bottom row.

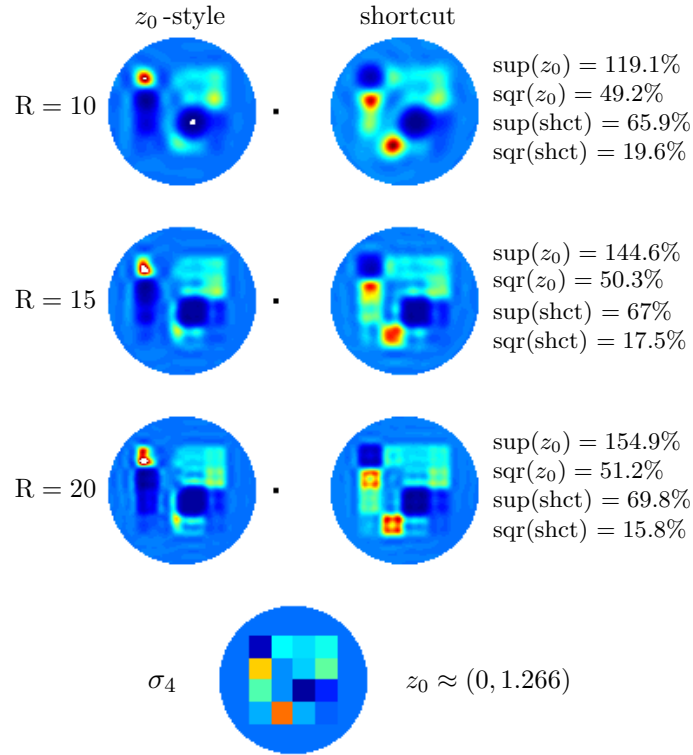


Figure 13: Comparison of reconstructions for σ_4 by the low-pass transport matrix method (left) and the shortcut method (right) using different cut-off frequencies R . The chosen point z_0 appears in black. The true conductivity is represented at the bottom row.

4.3. Numerical evidence of the transport matrix efficiency. In addition, further numerical experiments were made aimed at comparing the actual complex geometric optics solution to the Beltrami equation

$$\bar{\partial}_z f_\mu(z, k_0) = \mu(z) \overline{\partial_z f_\mu(z, k_0)}, \quad \text{for } z \in \Omega, \quad k_0 = 1,$$

and the transported solution $\tilde{f}_\mu(z, k_0)$ to the unit disc from $f_\mu(z_0, k_0)$ and $f_{-\mu}(z_0, k_0)$ at certain $z_0 \in \mathbb{C} \setminus \bar{\Omega}$.

Figure 14 shows some pictures for $f_\mu(z, k_0)$ and $\tilde{f}_\mu(z, k_0)$ corresponding to the conductivity example σ_4 . Here $|z| < 1$, $k_0 \approx 1$ and the pivot point outside the unit disc is $z_0 \approx (0, 1.266)$. To compute \tilde{f}_μ the transport matrix was generated with a cut-off frequency $R = 20$ and we took the size parameters as follows: $m_k = 7$, $m_z = 7$, $s_z = 1.5$.

The relative errors with sup and l^2 norms

$$\text{sup} := \frac{\left\| f_\mu(\cdot, k_0) - \tilde{f}_\mu(\cdot, k_0) \right\|_{l^\infty}}{\left\| f_\mu(\cdot, k_0) \right\|_{l^\infty}} \cdot 100 \%, \quad \text{sqr} := \frac{\left\| f_\mu(\cdot, k_0) - \tilde{f}_\mu(\cdot, k_0) \right\|_{l^2}}{\left\| f_\mu(\cdot, k_0) \right\|_{l^2}} \cdot 100 \%$$

are

$$(4.4) \quad \text{sup} = 20.23\%, \quad \text{sqr} = 10.28\%,$$

respectively.

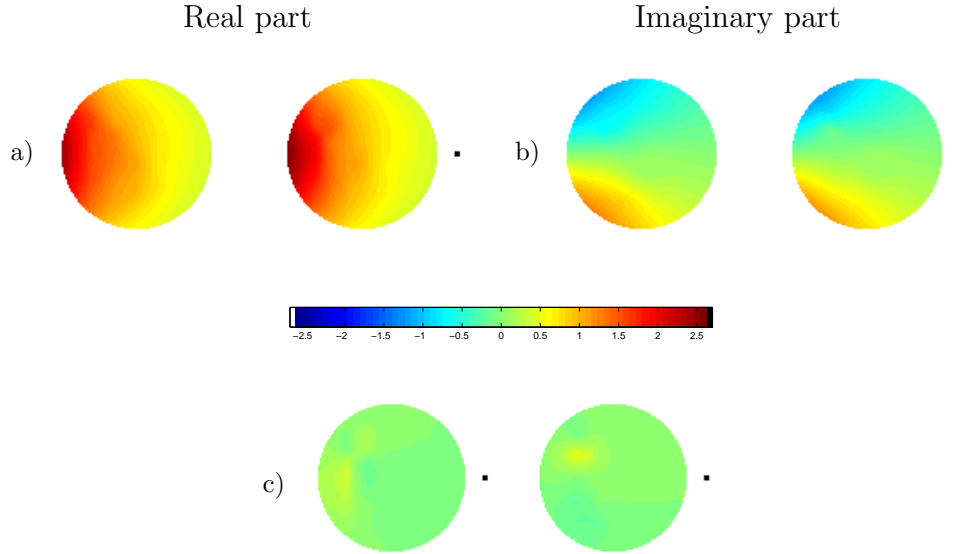


Figure 14: Comparison of $f_\mu(z, k_0)$ and $\tilde{f}_\mu(z, k_0)$ for the conductivity σ_4 with $R = 20$. In the first row we show real and imaginary parts of both functions. In a) the real part of the actual solution $f_\mu(z, k_0)$ is depicted on the left and the real part of the transported $\tilde{f}_\mu(z, k_0)$ on the right (where the point z_0 is represented in black). In b) the same information is showed for the imaginary part of $f_\mu(z, k_0)$ and $\tilde{f}_\mu(z, k_0)$. The last row c) shows the difference $\tilde{f}_\mu(z, k_0) - f_\mu(z, k_0)$. The real part is exhibited on the left and the imaginary part on the right. Again, the pivot point z_0 appears in black. All the pictures were generated under the same colormap using Matlab.

5. CONCLUSION

Regarding the radially symmetric examples studied in Section 4.1, the conclusion is clear: numerical evidence suggests that discontinuous conductivities can be reconstructed with the shortcut method more and more accurately when R tends to infinity.

The errors in the reconstructions are very similar to the Gibbs phenomenon observed with truncated linear Fourier transforms.

The numerical study of the nonsymmetric examples comparing both reconstruction types leads us to two observations:

- For these discontinuous conductivity examples, the shortcut method generates considerably better reconstructions than the transport matrix method.

- The approximate solution computed by the transport matrix method is reliable on an area within the unit disc close enough to the selected z_0 point outside the unit disc.

Finally, since errors (4.4) are small and plots for both functions $f_\mu(z, k_0)$, $\tilde{f}_\mu(z, k_0)$ are similar in view of Figure 14, we have numerical evidence supporting the fact that the transport matrix method “transports well” and the worse results by the transport matrix method are explained by the final algebraic steps, including numerical differentiation in (3.12), just after the computation of the solutions $u_1^{(R)}(z, k_0)$, $u_2^{(R)}(z, k_0)$ in (3.11) through the transport matrix itself.

APPENDIX

This Appendix is aimed at presenting two final discussions as follows. On a hand, the noisy scattering transform referred to in Section 3.2 is compared with the free-noise scattering transform computed by solving the Beltrami equation and formula (2.4) for the checkerboard-style conductivity phantom σ_3 from Figure 9. On the other hand, a quantitative discussion on the precision required to the DN map to obtain the accuracy of the scattering transform on the disc of radius 50 is introduced.

Example of noisy scattering transforms

For simplicity of notation, let us write τ_p for the scattering data obtained on the disc centered at the origin of radius 6 by solving the boundary integral equation mentioned in Section 3.1 from a simulated Dirichlet-to-Neumann map, Λ^p , with $p\%$ noise. Additionally, denote by τ the aforementioned free-noise scattering transform on the same disc (denoted by τ_3^{SC} in Section 4.2).

The approximate Dirichlet-to-Neumann map Λ^p is computed adding $p\%$ Gaussian noise to the FEM boundary voltages (for σ_3) as it is explained in Section 5.3 of [20].

The k -grid consists of $2^{m_k} \times 2^{m_k}$ equispaced points in the square $[-6, 6]^2$ with $m_k = 7$. The scattering data are computed on the 12,851 points of such grid belonging to the disc of radius 6. For the grid in the z -variable used to compute τ , $2^{m_z} \times 2^{m_z}$ equidistributed points are taken in the square $[-s_z, s_z]^2$, with step $h_z = s_z/2^{m_z-1}$ and $s_z = 2.3$.

For different choices of p the following absolute error is computed for r varying over a partition of the interval $(0, 6]$:

$$E_p(r) := \left\| \chi_{D(0,r)}(\tau - \tau_p) \right\|_{L^\infty} ,$$

where $\chi_{D(0,r)}$ denotes the characteristic function of the disc centered at the origin and radius r .

In Figure 15 the profiles of $E_p(r)$ for $p = 0.1\%$, 0.5% , 1% , 5% are shown in black, blue, green and red colour, respectively. The maximum value shown on the vertical axis is 1.

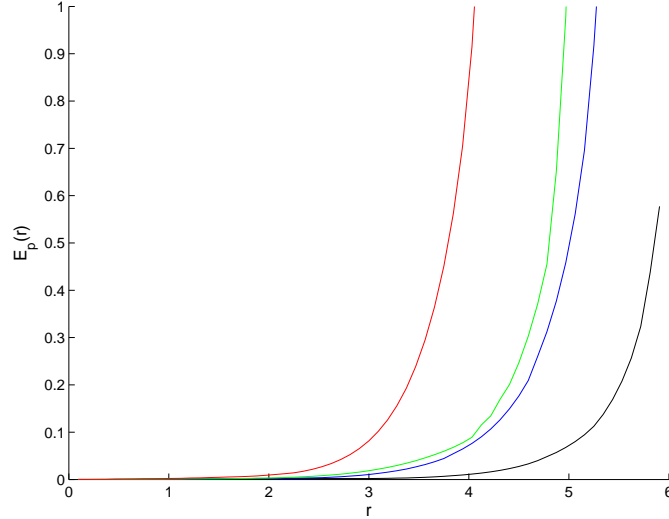


Figure 15: Profiles of the values of $E_p(r)$ in $(0, 1)$ with $r \in (0, 6)$, for $p = 0.1\%$ (black), $p = 0.5\%$ (blue), $p = 1\%$ (green), $p = 5\%$ (red).

Accuracy of the DN map to compute $\mathbf{t}(k)$ on $D(0, 50)$

How many correct significant digits would one need in the DN map for computing the scattering transform $\mathbf{t}(k)$ for $|k| < 50$? It is well-known [1] that there is a logarithmic relation between measurement accuracy and details in conductivity. In other words, EIT is an exponentially ill-posed inverse problem. In terms of scattering transforms, a fixed noise level $p\%$ in the EIT measurement leads to, roughly speaking, the computation of $\mathbf{t}(k)$ to be stable and accurate in a disc $|k| < R(p)$ and unstable outside that disc. See [34, Figure 2]. The exponential ill-posedness shows up as a logarithmic dependence of R on p , see [34, Figure 3]. Improving the measurement accuracy so that the DN matrix entries have one more significant digit increases the stability radius from R to $R + \Gamma$ with $\Gamma > 0$ a fixed real number.

Let us make a crude quantitative estimation based on [34, Figure 3]. Two significant digits in the DN map corresponds to $R = 3$ and six significant digits to $R = 7$. A quick computation shows that achieving the stability radius $R = 50$ would require 49 correct significant digits in the elements of the DN matrix (and, actually, using a larger matrix with more oscillatory basis functions involved as well).

Acknowledgements. This work was supported by the Finnish Centre of Excellence in Inverse Problems Research 2012-2017 (Academy of Finland CoE-project 250215). In addition, KA was supported by Academy of Finland, projects 75166001 and 1134757, and LP was supported by ERC-2010 Adv. Grant, 267700 - InvProb. The third author was also partially supported by Academy of Finland (Decision number 141075) and Ministerio de Ciencia y Tecnología de España (project MTM 2011-02568).

REFERENCES

- [1] G. ALESSANDRINI, *Stable Determination of Conductivity by Boundary Measurements*, *Applicable Analysis*, 27 (1988), pp. 153–172.
- [2] K. ASTALA, T. IWANIEC, AND G. MARTIN, *Elliptic partial differential equations and quasiconformal mappings in the plane*, vol. 48 of Princeton Mathematical Series, Princeton University Press, Princeton, NJ, 2009.
- [3] K. ASTALA, J. MUELLER, L. PÄIVÄRINTA, A. PERÄMÄKI, AND S. SILTANEN, *Direct electrical impedance tomography for nonsmooth conductivities*, *Inverse Problems and Imaging*, 5 (2011), pp. 531–549.
- [4] K. ASTALA, J. MUELLER, L. PÄIVÄRINTA, AND S. SILTANEN, *Numerical computation of complex geometrical optics solutions to the conductivity equation*, *Applied and Computational Harmonic Analysis*, 29 (2010), pp. 391–403.
- [5] K. ASTALA AND L. PÄIVÄRINTA, *A boundary integral equation for Calderón’s inverse conductivity problem*, in *Proc. 7th Internat. Conference on Harmonic Analysis, Collectanea Mathematica*, 2006.
- [6] K. ASTALA AND L. PÄIVÄRINTA, *Calderón’s inverse conductivity problem in the plane*, *Annals of Mathematics*, 163 (2006), pp. 265–299.
- [7] R. M. BROWN AND G. UHLMANN, *Uniqueness in the inverse conductivity problem for nonsmooth conductivities in two dimensions*, *Communications in Partial Differential Equations*, 22 (1997), pp. 1009–1027.
- [8] M. BRÜHL, *Explicit characterization of inclusions in electrical impedance tomography*, *SIAM Journal on Mathematical Analysis*, 32 (2001), pp. 1327–1341.
- [9] M. BRÜHL AND M. HANKE, *Numerical implementation of two non-iterative methods for locating inclusions by impedance tomography*, *Inverse Problems*, 16 (2000), pp. 1029–1042.
- [10] A.-P. CALDERÓN, *On an inverse boundary value problem*, in *Seminar on Numerical Analysis and its Applications to Continuum Physics (Rio de Janeiro, 1980)*, *Soc. Brasil. Mat.*, Rio de Janeiro, 1980, pp. 65–73.
- [11] P. CARO, A. GARCÍA, AND J. M. REYES, *Stability of the Calderón problem for less regular conductivities*, *Journal of Differential Equations*, 254 (2013), pp. 469–492.
- [12] M. CHENEY, D. ISAACSON, AND J. C. NEWELL, *Electrical impedance tomography*, *SIAM Review*, 41 (1999), pp. 85–101.
- [13] A. CLOP, D. FARACO, AND A. RUIZ, *Stability of Calderón’s inverse conductivity problem in the plane for discontinuous conductivities*, *Inverse Problems and Imaging*, 4 (2010), pp. 49–91.
- [14] R. CROKE, J. L. MUELLER, M. MUSIC, P. PERRY, S. SILTANEN, AND A. STAHEL, *The Novikov-Veselov equation: Theory and computation*, arXiv preprint, arXiv:1312.5427, (2013).
- [15] D. FARACO AND K. ROGERS, *The Sobolev norm of characteristic functions with applications to the Calderón Inverse Problem*, *The Quarterly Journal of Mathematics*, 64 (2013), pp. 133–147.

- [16] A. FRIEDMAN, *Detection of mines by electric measurements*, SIAM Journal on Applied Mathematics, 47 (1987), pp. 201–212.
- [17] B. GEBAUER AND N. HYVÖNEN, *Factorization method and inclusions of mixed type in an inverse elliptic boundary value problem*, Inverse Problems and Imaging, 2 (2008), pp. 355–372.
- [18] B. HABERMAN AND D. TATARU, *Uniqueness in Calderón’s problem with Lipschitz conductivities*, Duke Mathematical Journal, 162 (2013), pp. 497–516.
- [19] S. HAMILTON, C. HERRERA, J. L. MUELLER, AND A. VON HERRMANN, *A direct D -bar reconstruction algorithm for recovering a complex conductivity in 2- D* , Arxiv preprint, (2012).
- [20] S. HAMILTON, M. LASSAS, AND S. SILTANEN, *A direct reconstruction method for anisotropic electrical impedance tomography*, Inverse Problems, to appear (arXiv preprint, arXiv:1402.1117).
- [21] M. HANKE AND B. SCHAPPEL, *The factorization method for electrical impedance tomography in the half-space*, SIAM Journal on Applied Mathematics, 68 (2008), pp. 907–924.
- [22] B. HARRACH AND J. K. SEO, *Detecting inclusions in electrical impedance tomography without reference measurements*, SIAM J. Appl. Math., 69 (2009), pp. 1662–1681.
- [23] B. HARRACH AND M. ULLRICH, *Monotonicity-based shape reconstruction in electrical impedance tomography*, SIAM J. Math. Anal., 45 (2013), pp. 3382–3403.
- [24] M. HUHTANEN AND A. PERÄMÄKI, *Numerical solution of the R -linear Beltrami equation*, Mathematics of Computation, 81 (2012), pp. 387–397.
- [25] N. HYVÖNEN, *Application of the factorization method to the characterization of weak inclusions in electrical impedance tomography*, Advances in Applied Mathematics, 39 (2007), pp. 197–221.
- [26] T. IDE, H. ISOZAKI, S. NAKATA, AND S. SILTANEN, *Local detection of three-dimensional inclusions in electrical impedance tomography*, Inverse problems, 26 (2010), p. 035001.
- [27] T. IDE, H. ISOZAKI, S. NAKATA, S. SILTANEN, AND G. UHLMANN, *Probing for electrical inclusions with complex spherical waves*, Communications on pure and applied mathematics, 60 (2007), pp. 1415–1442.
- [28] M. IKEHATA AND S. SILTANEN, *Numerical method for finding the convex hull of an inclusion in conductivity from boundary measurements*, Inverse Problems, 16 (2000), pp. 1043–1052.
- [29] M. IKEHATA AND S. SILTANEN, *Electrical impedance tomography and Mittag-Leffler’s function*, Inverse Problems, 20 (2004), pp. 1325–1348.
- [30] D. ISAACSON, J. MUELLER, J. NEWELL, AND S. SILTANEN, *Imaging cardiac activity by the D -bar method for electrical impedance tomography*, Physiological Measurement, 27 (2006), pp. S43–S50.
- [31] D. ISAACSON, J. L. MUELLER, J. C. NEWELL, AND S. SILTANEN, *Reconstructions of chest phantoms by the D -bar method for electrical impedance tomography*, IEEE Transactions on Medical Imaging, 23 (2004), pp. 821–828.
- [32] K. KNUDSEN, *A new direct method for reconstructing isotropic conductivities in the plane*, Physiological Measurement, 24 (2003), pp. 391–403.
- [33] K. KNUDSEN, M. LASSAS, J. MUELLER, AND S. SILTANEN, *D -bar method for electrical impedance tomography with discontinuous conductivities*, SIAM Journal on Applied Mathematics, 67 (2007), p. 893.
- [34] K. KNUDSEN, M. LASSAS, J. MUELLER, AND S. SILTANEN, *Regularized D -bar method for the inverse conductivity problem*, Inverse Problems and Imaging, 3 (2009), pp. 599–624.
- [35] K. KNUDSEN, J. MUELLER, AND S. SILTANEN, *Numerical solution method for the d -bar equation in the plane*, Journal of Computational Physics, 198 (2004), pp. 500–517.

- [36] K. KNUDSEN AND A. TAMASAN, *Reconstruction of less regular conductivities in the plane*, Communications in Partial Differential Equations, 29 (2004), pp. 361–381.
- [37] M. LASSAS, J. L. MUELLER, S. SILTANEN, AND A. STAHEL, *The Novikov-Veselov Equation and the Inverse Scattering Method: II. Computation*, Nonlinearity, 25 (2012), pp. 1799–1818.
- [38] ———, *The Novikov-Veselov Equation and the Inverse Scattering Method, Part I: Analysis*, Physica D, 241 (2012), pp. 1322–1335.
- [39] A. LECHLEITER, N. HYVÖNEN, AND H. HAKULA, *The factorization method applied to the complete electrode model of impedance tomography*, SIAM Journal on Applied Mathematics, 68 (2008), pp. 1097–1121.
- [40] J. MUELLER AND S. SILTANEN, *Direct reconstructions of conductivities from boundary measurements*, SIAM Journal on Scientific Computing, 24 (2003), pp. 1232–1266.
- [41] ———, *Linear and Nonlinear Inverse Problems with Practical Applications*, SIAM, 2012.
- [42] M. MUSIC, P. PERRY, AND S. SILTANEN, *Exceptional circles of radial potentials*, Inverse Problems, 29 (2013).
- [43] A. I. NACHMAN, *Global uniqueness for a two-dimensional inverse boundary value problem*, Annals of Mathematics, 143 (1996), pp. 71–96.
- [44] P. A. PERRY, *Miura Maps and Inverse Scattering for the Novikov-Veselov Equation*, ArXiv e-prints 1201.2385, (2012).
- [45] S. SILTANEN, J. MUELLER, AND D. ISAACSON, *An implementation of the reconstruction algorithm of A. Nachman for the 2-D inverse conductivity problem*, Inverse Problems, 16 (2000), pp. 681–699.
- [46] G. UHLMANN AND J.-N. WANG, *Reconstructing discontinuities using complex geometrical optics solutions*, SIAM J. Appl. Math., 68 (2008), pp. 1026–1044.
- [47] G. VAINIKKO, *Fast solvers of the Lippmann-Schwinger equation*, in Direct and inverse problems of mathematical physics (Newark, DE, 1997), vol. 5 of Int. Soc. Anal. Appl. Comput., Kluwer Acad. Publ., Dordrecht, 2000, pp. 423–440.